Three-dimensional model for gas tungsten arc welding with filler metal

H G Fan and R Kovacevic

Proceedings of the Institution of Mechanical Engineers, Part B: Journal of Engineering Manufacture 2006 220: 1107
DOI: 10.1243/09544054JEM406

Three-dimensional model for gas tungsten arc welding with filler metal

H G Fan* and **R Kovacevic**
School of Engineering, Southern Methodist University, Richardson, Texas, USA

The manuscript was received on 12 June 2005 and was accepted after revision for publication on 29 March 2006.

DOI: 10.1243/09544054JEM406

Abstract: This paper presents a three-dimensional model to describe the transient heat and fluid flow in gas tungsten arc welding (GTAW) with a filler metal. Using the volume of fluid (VOF) method, the melt depth and the surface profile of the weld are predicted. The GTAW experiments show that the predictions of the weld pool shape based on the model are in good agreement with the measured values.

Keywords: gas tungsten arc welding, filler metal, volume of fluid, three-dimensional modelling

1 INTRODUCTION

Gas tungsten arc welding (GTAW) is an arc welding process that uses an arc between a non-consumable tungsten electrode and the weld pool. The metal to be welded is melted by the intense heat of the arc and fuses together either with (Fig. 1) or without a filler metal. Once the arc and weld pool are established, the torch is moved along the joint line. The arc progressively melts the base metal and, if it is used, the filler metal. The GTAW process produces a superior quality weld with almost all metals and allows precise control, thus it is widely used. In order to achieve a certain weld quality, a list of suitable welding parameters and their combinations must be chosen. The most influential welding parameters include the welding current, arc length, wire feeding rate, and welding speed [**1**]. The welding current corresponds to the amount of heat applied to the part. Welding current also affects the voltage, with the voltage (at a fixed arc length) increasing with the current. Arc length is important because it also affects the width of the weld pool. Wire feeding speed determines the amount of filler deposited per unit length of weld. Decreasing wire feeding speed will increase penetration and flatten the bead contour. Welding speed affects both the width and penetration. A lower welding speed means more heat input per unit length of weld. A numerical model provides the capability to select suitable welding parameters and predict the weld shape. The model also makes clear the complicated arc welding phenomena.

In view of the significant effect of the weld pool convection on the microstructure and properties of the resultant weld, numerous investigators have attempted to calculate the heat transfer and fluid flow in the weld pool, especially in GTAW [**2**–**5**]. For GTAW, convection in the weld pool is driven by a combination of forces, which include surface tension force, buoyancy force, electromagnetic force, and arc drag force. Kim *et al.* [**6**] investigated the effect of various driving forces on heat and mass transfer in gas tungsten arc (GTA) weld pool. In most cases, the fluid flow and heat transfer in the weld pool are controlled by the surface tension force [**7**]. Choo and Szekely [**8**] first considered turbulence in the simulation of the fluid flow in GTA weld pools and showed it can affect the pool depth. The surface active element was proved to affect the flow pattern in the weld pool and was used to increase the depth of penetration [**9**]. Fan and Tsai [**10**] simulated the dynamic movement of the molten pool from partial until full penetration.

The arc movement introduces three-dimensionality in the weld pool. Such effects were first addressed by Kou and Wang [**11**]. Zacharia *et al.* [**12**] considered the same configuration but included a number of additional effects, such as the curvature of the weld pool free surface and a turbulence model. Dutta *et al.* [**13**] considered the non-axisymmetric

**Corresponding author: Research Center for Advanced Manufacturing, Southern Methodist University, 1500 International Parkway, Suite 100, Richardson, TX 75081, USA. email: honggang_fan@yahoo.com*

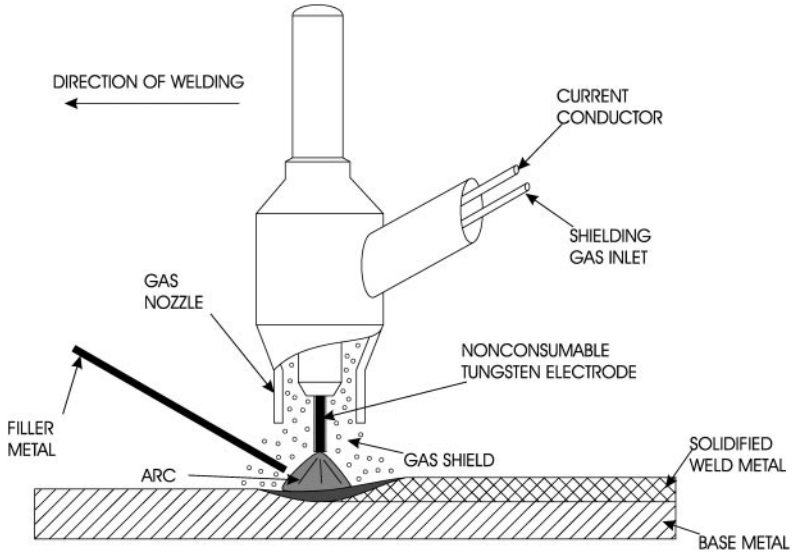

Fig. 1 Schematic diagram of GTAW torch and process

boundary conditions in the calculation of Lorentz forces for moving GTAW. Reddy *et al.* [**14**] used the finite element method to simulate three-dimensional heat transfer in pulsed GTAW; the fluid flow in the weld pool was not included in the model. In 1998, Cao *et al.* [**15**] incorporated full penetration and free top and bottom surfaces in a three-dimensional model with a moving GTAW heat source. Using boundary-fitted coordinates, Kim and Na [**16**] presented a three-dimensional quasi-steady model for the moving bead-on-plate gas metal arc welding (GMAW) process. The size and profile of the weld pool were predicted, but the dynamic interaction between the droplet and the weld pool free surface was not considered. Ushio and Wu [**17**] approximated the effect of the droplets on the weld pool as a constant force acting on the weld pool free surface, although the impingement process is not a continuous process. Recently, the transient development and diminution of the weld pool at two periods after the arc ignites and extinguishes have been analysed quantitatively by Wu and Yan [**18**]; the time for the weld pool shape to reach the quasi-steady state and the time for the weld pool to solidify completely are predicted. The model by Wu and Yan assumes the surface of the molten pool to be flat. Wang and Tsai [**19**] used the volume of fluid (VOF) algorithm to simulate the impingement of droplets in three-dimensional moving GMAW; the size of the droplets is predetermined, and the distribution of heat and current density on the top surface are assumed.

So far, no open literature has been found to present a dynamic model describing the GTAW with a feeding wire. The problem is very complicated by the following physical phenomena: the heat source is moving; the wire moves in the feeding direction and moves with the heat source; the feeding wire interacts with the free surface of weld pool; and volume of the weld pool is increased owing to the addition of molten metal droplets. In the current paper, a three-dimensional model has been developed to describe the transient heat and fluid flow in GTAW with a feeding wire. The melt depth and the surface profile are predicted. The GTAW experiment shows that the predictions of the weld pool shape based on the model are in good agreement with the measured values.

2 MATHEMATICAL MODEL

2.1 Governing equations

The following assumptions have been adopted for simplification.

1. The flow is Newtonian, incompressible, and laminar since the size of the pool is small [**6**, **15**, **18**, **20**].
2. Since the changes of material properties with temperature are not significant and the results are not sensitive to these changes [**15**, **20**], to simplify the problem, the physical properties of mild steel listed in Table 1 are assumed to be constant.
3. The wire is assumed to be always in touch with the substrate. In the actual GTAW after arc ignition, the wire and the substrate are both preheated by the arc plasma before the wire touches the substrate. Thus, it is reasonable to assume that they are in touch and are heated together even in the early phase of welding.

Table 1 Physical properties of the workpiece

Symbol	Value	Symbol	Value
β	$10^{-4}\,K^{-1}$	ρ	$7200\,kg/m^3$
γ	1.2 N/m	μ_0	1.26×10^{-6} H/m
μ	0.006 kg/m s	σ	$7.7\times10^5\,\Omega$/m
$d\gamma/dT$	10^{-4} N/m K	ε	0.9
C_p	753 J/kg K	ΔH	2.47×10^5 J/kg
T_l	1723 K	T_s	1523 K
k	20 W/m K	K_{max}	$10^4\,s^{-1}$

The governing equations for the fluid flow and heat transfer that occur in the weld pool are defined as follows.

Mass conservation

$$\frac{\partial(\rho)}{\partial t}+\nabla\bullet(\rho\boldsymbol{u})=0 \tag{1}$$

Momentum conservation

$$\frac{\partial}{\partial t}(\rho\boldsymbol{u})+\nabla\bullet(\rho\boldsymbol{u}\boldsymbol{u})=-\nabla p+\mu\nabla^2\boldsymbol{u}-K\boldsymbol{u}+\boldsymbol{J}\times\boldsymbol{B}+\rho g\beta(T-T_r)\boldsymbol{z} \tag{2}$$

The Lorentz force $\boldsymbol{J}\times\boldsymbol{B}$, buoyancy force $\rho g\beta(T-T_r)\boldsymbol{z}$ and temperature-dependent drag term $K\boldsymbol{u}$ that represents the fluid flow in the mushy zone are incorporated into the momentum equation where

$$K=\begin{cases}0 & T>T_l\\ K_{max}(T_l-T)/(T_l-T_s) & T_s\leqslant T\leqslant T_l\\ \infty & T<T_s\end{cases} \tag{3}$$

The effects of Lorentz force and buoyancy force are detailed in reference [**6**]. The drag term will obviously slow down the fluid velocity in the mushy zone.

Energy conservation

$$\frac{\partial}{\partial t}(\rho h)+\nabla\bullet(\rho\boldsymbol{u}h)=\nabla\bullet\left(\frac{k}{C_p}\nabla h\right)-\Delta H\frac{\partial f_L}{\partial t} \tag{4}$$

The latent heat will be absorbed or released when phase change, melting, or solidifying occurs. The latent heat of fusion ΔH is included by employing the liquid fraction f_L, which is defined as follows

$$f_L=\begin{cases}1 & T>T_l\\ (T-T_s)/(T_l-T_s) & T_s\leqslant T\leqslant T_l\\ 0 & T<T_s\end{cases} \tag{5}$$

where T_l and T_s are the liquidus and solidus temperature, respectively.

Conservation of electrical charge The electromagnetic force terms in equation (2) can be obtained by solving a steady state version of Maxwell's equations in the domain of the workpiece. The electric potential ϕ is calculated by solving the equation for current continuity

$$\nabla^2\phi=0 \tag{6}$$

and current density is calculated from Ohm's law

$$\boldsymbol{J}=-\sigma\nabla\phi \tag{7}$$

The magnetic flux density $\boldsymbol{B}$ is then obtained from

$$\nabla\times\boldsymbol{B}=\mu_0\boldsymbol{J} \tag{8}$$

Tracking of free surfaces

$$\frac{\partial F}{\partial t}+\nabla\bullet(\boldsymbol{u}F)=0 \tag{9}$$

The moving free surface is tracked using a volume of fluid function, F, which represents the volume of fluid in the computational cell. The function F takes the value of 1 for the cell filled with the fluid and becomes 0 for the empty cell. If the cell is located on the free surface, the function F has a value between 0 and 1.

In addition, there are some numerical techniques to handle the free surface such as surface pressure due to curvature. These are discussed in detail by Nichols *et al.* [**21**] and will not be reiterated here.

2.2 Boundary conditions

At the symmetrical $y=0$ plane, the following boundary conditions are used: a zero y direction velocity (v) at the plane and zero gradients of all other variable conditions normal to the plane. The velocities at all the surfaces except the top surface are set to 0. At the top surface, the temperature-dependent Marangoni force [**20**] in a direction tangential to the local free surface is given by

$$\tau_s=\mu\frac{\partial V_s}{\partial n}=\frac{d\gamma}{dT}\frac{\partial T}{\partial s} \tag{10}$$

where τ_s is the flow stress tensor, n and s are normal and tangential direction along the liquid metal surface, and γ is the temperature-dependent surface tension.

For the boundary conditions pertaining to the heat transfer problem at the top surface of the molten pool, although the filler metal affects the symmetry, in order to simplify the problem the heat flux from the welding arc is still assumed to obey a Gaussian type distribution of the form

$$-k\frac{\partial T}{\partial n}=\frac{\eta UI}{2\pi r_q^2}\exp\left[-\frac{(x-x_0)^2+y^2+(z-z_0)^2}{2r_q^2}\right]-h_c(T-T_\infty) \tag{11}$$

where $(x_0, 0, z_0)$ is the coordinate of the arc centre, x of arc centre is moving at the travelling speed, y of

arc centre is always 0, and z is varied according to the free surface. h_c is a combined heat loss coefficient owing to convection and radiation, as expressed in the following equation [**2**]

$$h_c = 24.1 \times 10^{-4} \varepsilon T^{1.61} \tag{12}$$

The boundary conditions for the surfaces without heat input are expressed as

$$-k\frac{\partial T}{\partial n} = h_c(T - T_\infty) \tag{13}$$

In order to solve the Maxwell equations, at the top surface, the assumed Gaussian type current flux is described by

$$-\sigma\frac{\partial \phi}{\partial n} = \frac{I}{2\pi r_c^2}\exp\left[-\frac{(x-x_0)^2 + y^2 + (z-z_0)^2}{2r_c^2}\right] \tag{14}$$

An iso-potential line ($\phi = 0$) is set at the bottom wall. All other surfaces are electrically insulated. In the current authors' calculation, the arc distribution parameters, i.e. η, r_q, and r_c, have been selected according to experimental results [**22**, **23**].

2.3 Numerical method

The governing equations with the boundary conditions are discretized using the control volume approach. Variables of the equations are solved iteratively using the VOF method modified to include heat transfer and the electromagnetic force. The numerical procedure is as follows.

1. Generate the grid, and set initial values.
2. Equation (6) is solved for the potential distribution Φ, and the values of Lorentz forces are obtained using equations (7) and (8).
3. Updated values of u, v, and P are obtained by equations (1) and (2) using the SIMPLE algorithm [**24**].
4. Update F described by equation (9) and determine the free surface.
5. Updated values of temperature are obtained from equation (4).
6. Return to step 2 and this loop is repeated until the convergence is achieved.

Convergence is achieved when the maximum absolute values of node mass residual at the end of each iteration are less than 10^{-4} and the maximum absolute values of the relative difference in potential and temperature at each node between successive iterations are less than 10^{-3}. A non-uniform grid of $150 \times 80 \times 70$ nodes is used for a computational domain of $20 \times 16 \times 10$ mm. The verification of grid and domain independence has been performed, and the grid and domain used are found to be suitable for the calculations.

3 RESULTS AND DISCUSSION

The welding was performed on a 4.8 mm thick mild steel plate with a welding current of 160 A. The wire used was a mild steel welding wire with a diameter of 1.2 mm. The shielding gas used was pure argon. The weld centreline was at $y = 0$ mm. The arc moved at a speed of 3.8 mm/s along the x direction with a starting point at $x = 5$ mm to avoid the end effects. The wire fed at a speed of 13.3 mm/s with an angle of 45° to the weld surface, and the arc centre was also the wire feeding position in the x direction. Figure 2 shows the three-dimensional weld pool surface at $t = 1.0$ s. Only part of the y coordinate is shown in Fig. 2. It can be seen that the weld bead is built up in the leading and trailing portion, except that a crater is shown in front of the wire owing to the push of the feeding wire.

Figure 3 is the side view showing the temperature and velocity distribution at $Y = 0$ surface. The highest temperatures appear on the surfaces of the base metal and wire that are near to the arc centre. The shapes of isotherms in the leading part of the weld pool are much thinner than the isotherms in the trailing part owing to the heat accumulation in the trailing part. The solidus temperature is drawn in the velocity distribution to show the boundary of the weld pool. It can be seen that the flow pattern in the side view of the weld pool is mainly determined by the feeding wire. As the welding time increases, both the weld pool length and depth increase. Compared with the change of the weld pool in the period of 1–1.5 s, the weld pool length and depth in the period of 1.5–2 s are increased slightly, i.e. the rate of increase in the weld pool size decreases as the time increases, since the pool size is closer to its quasi-steady state condition.

The temperature and velocity fields at the cross-section of $x = 8$ mm are shown in Fig. 4. At $t = 1$ s, the arc centre is close to $x = 9$ mm. The higher temperature appears on the top part. It is shown that the molten metal on the top surface flows radially inward and moves vertically upward near the z axis. That movement suggests the flow pattern in the cross-section of the weld pool is mainly determined by the Marangoni force owing to the variation of the surface tension coefficient with temperature. The Marangoni force acts inward on the molten surface with the higher temperature inside. As the arc plasma moves away, the size of the weld pool and the value of velocity are decreased at $t = 1.5$ s. The solidification front line moves towards the top areas around the z axis gradually, suggesting the heat loss is mainly from the solid metal. It is seen that the cross-section is completely solidified at $t = 2$ s.

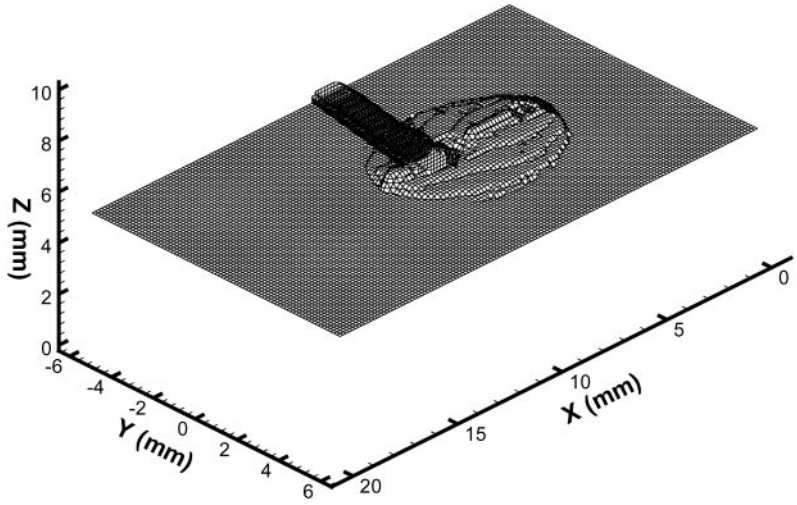

Fig. 2 Partial view of a three-dimensional weld pool surface at $t = 1.0$ s

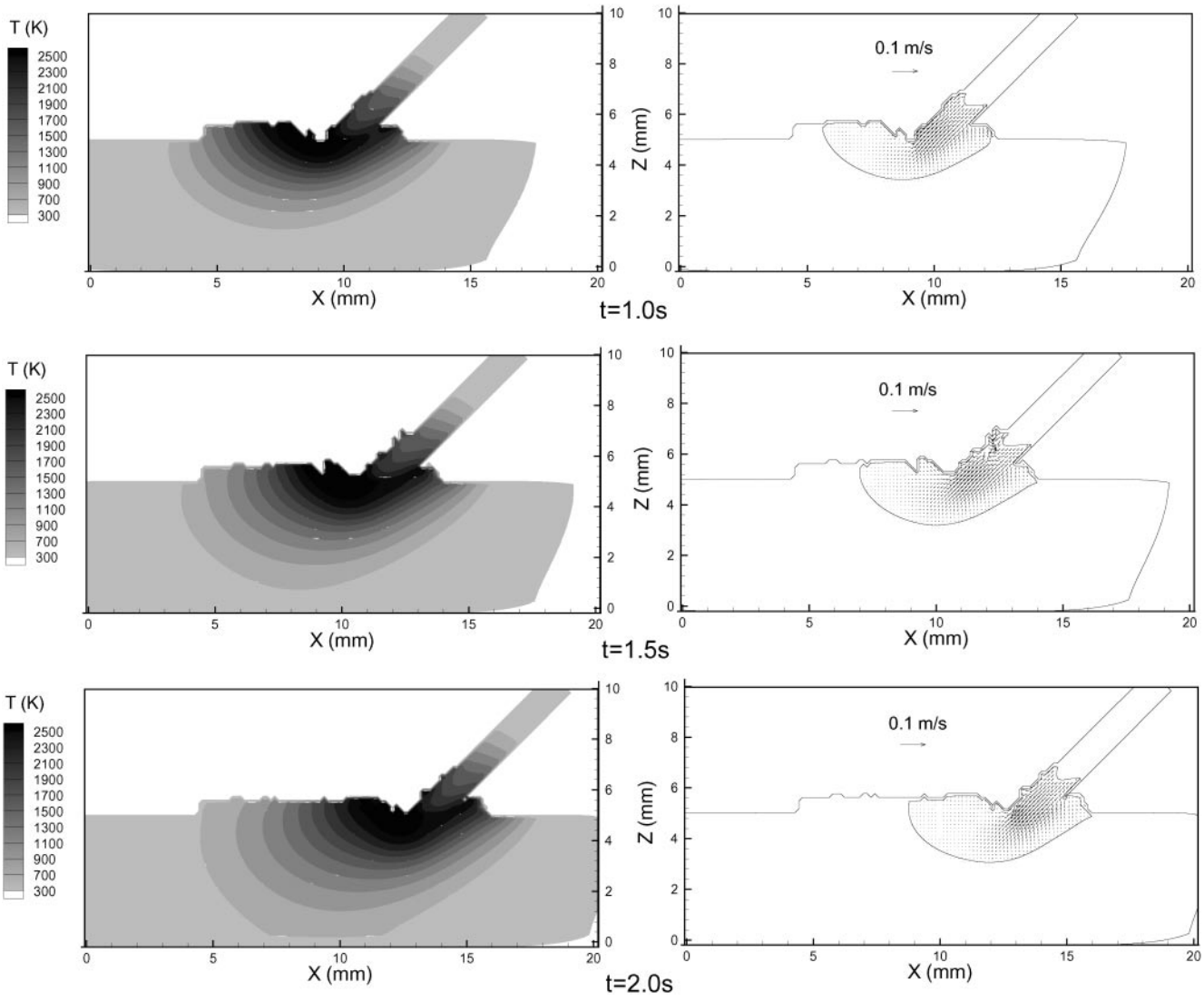

Fig. 3 Temperature and velocity distributions at $y = 0$ mm

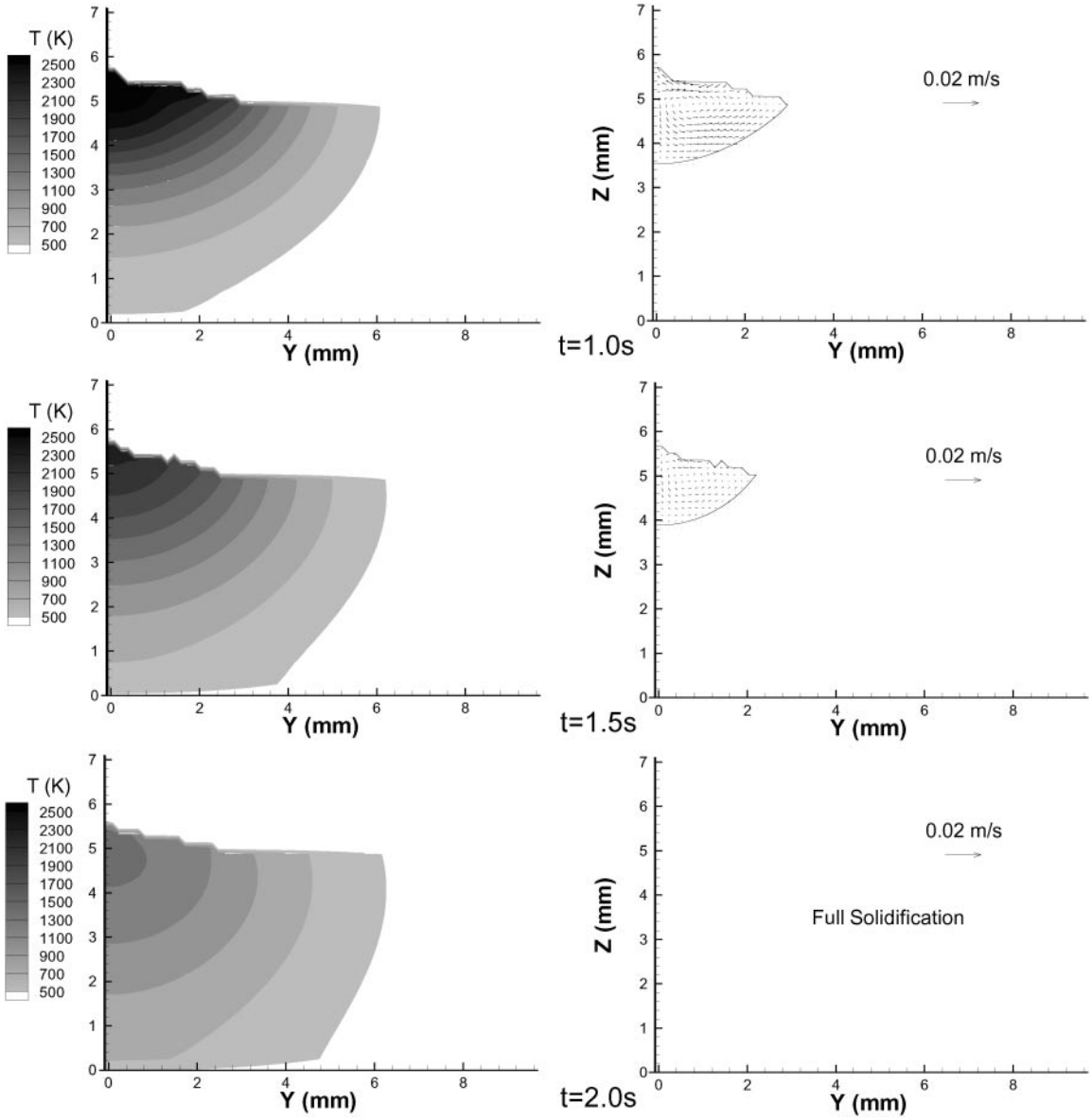

Fig. 4 Temperature and velocity distributions at $x = 8$ mm

The top view of the weld at $z = 4.8$ mm is shown in Fig. 5. The higher temperatures appear under the arc centre. The width of the weld pool is not increased very much after 1 s. The length of the weld pool is continuously increased owing to the heat accumulation along the x direction. Also, the increase in length is mainly behind the arc centre, i.e. the ratio between the leading and trailing portions of the weld pool decreases with increase in time. In addition, it is seen that the molten metal from the feeding wire dominates the velocity distribution around the arc centre.

The experimental cross-section of weld bead is shown in Fig. 6. The bead build-up B_b, the bead width B_w, and the depth of penetration D_p are compared with the calculation results. It can be seen from Table 2 that the predicted results are in reasonable agreement with the experiment. The length (80 mm) of the experimental workpiece is much longer than the computation domain. The experimental cross-section of the weld bead is taken from the middle of the whole weld bead, which is at the quasi-steady state. Multiple experiments have been conducted under the same welding parameters and the results shown in Fig. 6 are very close to the average values.

4 CONCLUSIONS

A three-dimensional model has been developed to analyse the heat and mass transfer in the GTAW

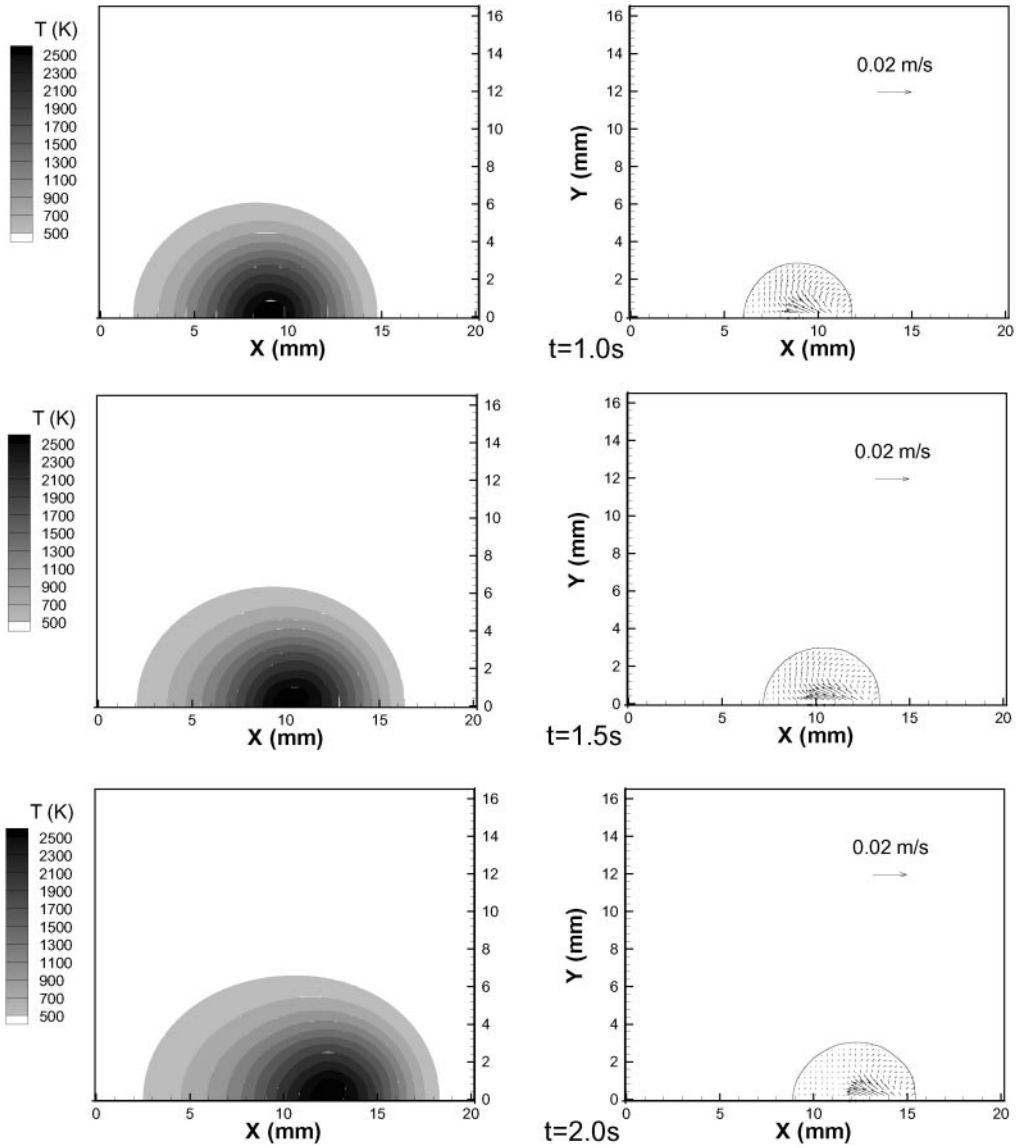

Fig. 5 Temperature and velocity distributions at $z = 4.8$ mm

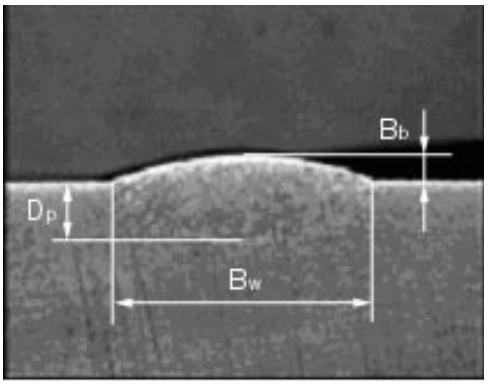

Fig. 6 Cross-section of the weld bead

weld pool with filler metal. The numerical results agree well with the experimental image. The principal conclusions are summarized as follows.

Table 2 Comparison of computational and experimental results

	B_w(±0.5 mm)	B_b (±0.5 mm)	D_p (±0.5 mm)
Calculation (Fig. 4)	5.0	0.6	1.4
Experiment (Fig. 6)	5.7	0.5	1.3

The rate of increase in the weld pool size decreases as the time increases. During the growth of weld pools, the width–length ratio of the weld pool and the ratio between the leading and trailing portions decrease.

The higher temperatures appear around the arc centre; the shapes of isotherms in the leading part are thinner than the isotherms in the trailing part. The velocity distribution around the arc centre is dominated by the feeding wire. The flow pattern in

the cross-section of the weld pool such as $x = 8$ mm is determined by the Marangoni force.

ACKNOWLEDGEMENT

This work was supported by the National Science Foundation under grant DMI-0320663 and THECB/ATP grant 003613-0016-2001, which is gratefully acknowledged.

REFERENCES

1 **American Welding Society.** *Welding handbook,* 9th Edition, 2000.
2 **Goldak, J., Bibby, M., Moore, J.,** and **Patel, B.** Computer modeling of heat flow in welds. *Metall. Trans. B,* 1986, **17B,** 587–600.
3 **Zacharia, T., David, S. A., Vitek, J. M.,** and **DebRoy, T.** Weld pool development during GTA and laser beam welding of type 304 stainless steel, Part I – theoretical analysis. *Welding J.*, 1989, **68**(12), 499s–509s.
4 **Zacharia, T., Eraslan, A. H.,** and **Aidun, D. K.** Modeling of non-autogenous welding. *Welding J.*, 1988, **67**(1), 18s–27s.
5 **Lee, S. Y.** and **Na, S. J.** Numerical analysis of molten pool convection considering geometric parameters of cathode and anode. *Welding J.*, 1997, **76**(11), 484s–497s.
6 **Kim, W. H., Fan, H. G.,** and **Na, S. J.** Effect of various driving forces on heat and mass transfer in arc welding. *Numer. Heat Transfer Part A,* 1997, **32**(6), 633–652.
7 **Zacharia, T., David, S. A., Vitek, J. M.,** and **Kraus, H. G.** Computational modeling of stationary gas-tungsten-arc weld pools and comparison to stainless steel 304 experimental results. *Metall. Mater. Trans. B,* 1991, **22B**, 243–257.
8 **Choo, R. T. C.** and **Szekely, J.** The possible role of turbulence in GTA weld pool behavior. *Welding J.*, 1994, **73**(2), 25s.
9 **Wang, Y.** and **Tsai, H. L.** Modeling of the effects of surface-active elements on flow patterns and weld penetration. *Metall. Mater. Trans. B,* 2001, **32B**, 145–161.
10 **Fan, H. G.** and **Tsai, H. L.** Heat transfer and fluid flow in a partially or fully penetrated gas tungsten arc welding. *Int. J. Heat Mass Transfer,* 2001, **44**(2), 417–428.
11 **Kou, S.** and **Wang, Y. H.** Computer simulation of convection moving arc weld pools. *Metall. Trans.*, 1986, **17A**, 2271.
12 **Zacharia, T., Eraslan, A. H.,** and **Aidun, K.** Modeling of autogenous welding. *Welding J.*, 1988, **67**, 53s–62s.
13 **Dutta, P., Joshi, Y.,** and **Janaswamy, R.** Thermal modeling of gas tungsten arc welding process with nonaxisymmetric boundary conditions. *Numer. Heat Transfer Part A,* 1995, **27**, 499–518.
14 **Reddy, A. C., Guha, B.,** and **Achar, D. R. G.** Finite element modeling of three-dimensional transient heat transfer in stainless steel (304) pulsed GTA weldments. *Numer. Heat Transfer Part A,* 2002, **41**, 41–64.
15 **Cao, Z. N., Zhang, Y. M.,** and **Kovacevic, R.** Numerical dynamic analysis of moving GTA weld pool. *J. Mfg Sci. Engng,* 1998, **120**, 173–177.
16 **Kim, J. W.** and **Na, S. J.** A study on the three-dimensional analysis of heat and fluid flow in GMAW using boundary-fitted coordinates. *Trans. ASME,* 1994, **116**(2), 78–85.
17 **Ushio, M.** and **Wu, C. S.** Mathematical modeling of three-dimensional heat and fluid flow in a moving gas metal arc weld pool. *Metall. Trans.*, 1997, **28B**, 509–517.
18 **Wu, C. S.** and **Yan, F. J.** Numerical simulation of transient development and diminution of weld pool in gas tungsten arc welding. *Modelling Simulation Mater. Sci. Engng,* 2004, **12**, 13–20.
19 **Wang, Y.** and **Tsai, H. L.** Modeling heat and mass transfer and fluid flow in three-dimensional gas metal arc welding. In Proceedings of IMECE'02: 2002 ASME International Mechanical Engineering Congress and Exposition, New Orleans, Louisiana, USA, 17–22 November 2002, pp. 1–16.
20 **Choo, R. T. C., Szekely, J.,** and **Westhoff, R. C.** Modeling of high-current arcs with emphasis on free surface phenomena in the weld pool. *Welding J.*, 1990, **69**, 346s–361s.
21 **Nichols, B. D., Hirt, C. W.,** and **Hotchkiss, R. S.** SOLA-VOF: a solution algorithm for transient fluid flow with multiple free boundaries. Report LA-8355, Los Alamos Scientific Laboratory, 1980.
22 **Patankar, S. V.** *Numerical Heat Transfer and Fluid Flow,* 1980 (Hemisphere, Washington DC).
23 **Lin, M. L.** and **Eagar, T. W.** Pressures produced by gas tungsten arcs. *Metall. Trans. B,* 1986, **17B**, 601–607.
24 **Dutta, P., Joshi, Y.,** and **Franche, C.** Determination of gas tungsten arc welding efficiencies. *Expl Thermal Fluid Sci.*, 1994, **9**, 80–89.

APPENDIX

Notation

B	magnetic flux density (Wb/m^2)
B_b	bead build-up (m)
B_w	bead width (m)
B_θ	azimuthal magnetic field (Wb/m^2)
C_p	heat capacity (J/kg K)
D_p	depth of penetration (m)
f_L	liquid fraction
F	volume of fluid
g	gravitational acceleration (m/s^2)
h	specific enthalpy (J/kg)
h_c	combined heat transfer coefficient at the surface (W/m^2 K)
I	arc current (A)
J	current density (A/m^2)
k	thermal conductivity (W/m K)
K	drag index in source term (kg/m^3 s)
K_{max}	maximum drag index (kg/m^3 s)
n, s	normal, tangential direction to surface (m)

P	pressure (Pa)
r_q, r_c	heat, current flux distribution radius (m)
t	time (s)
T	temperature (K)
T_l	liquidus temperature (K)
T_m	melting temperature (K)
T_r	reference temperature (K)
T_s	solidus temperature (K)
T_∞	surrounding temperature (K)
u	velocity (m/s)
U	arc voltage (V)
V_n	normal velocity component at molten pool surface (m/s)
V_s	tangential velocity component at molten pool surface (m/s)
V_w	wire feed speed (m/s)
x_o	x coordinate of arc centre (m)
z_o	z coordinate of arc centre (m)
β	coefficient of thermal expansion (1/K)
γ	surface tension (N/m)
$d\gamma/dT$	temperature gradient of surface tension (N/K m)
ε	emissivity of body surface
ΔH	latent heat of fusion (J/kg)
η	arc efficiency (%)
μ	viscosity (kg/m s)
μ_o	permittivity of free space (H/m)
ρ	density (kg/m^3)
σ	electrical conductivity (1/Ω m)
τ_s	Marangoni shear stress (Pa)
ϕ	electric potential (V)